Local Cation Ordering in Compositionally Complex Ruddlesden-Popper $n = 1$ Oxides

Bo Jiang, Krishna Chaitanya Pitike, De-Ye Lin, Stephen C. Purdy, Xin Wang, Yafan Zhao, Yuanpeng Zhang, Peter Metz, Antonio Macias, Harry M. Meyer, Albina Y. Borisevich, Jiaqiang Yan, Valentino R. Cooper, Craig A. Bridges, Katharine Page*

Dr. B. Jiang, Dr. S. C. Purdy, Dr. Y. Zhang, Dr. A Macias, Prof. K. Page
Neutron Scattering Division, Oak Ridge National Laboratory, Oak Ridge, Tennessee, 37831, United States
Email Address:kpage10@utk.edu
Dr. K. C. Pitike, Dr. V. R. Cooper, Dr. H. M. Meyer, Dr. J. Yan
Materials Sciences and Technology Division, Oak Ridge National Laboratory, Oak Ridge, Tennessee, 37831, United States
Dr. K. C. Pitike
Nuclear Sciences Division, Pacific Northwest National Laboratory, Richland, Washington 99352, United States
Mr. A. Macias
Department of Chemistry, University of California, Los Angeles, California 94720, United States
Dr. A. Y. Borisevich
Center for Nanophase Materials Sciences, Oak Ridge National Laboratory, Oak Ridge, Tennessee, 37831, United States
Dr. D. Lin, Dr. Y. Zhao
Institute of Applied Physics and Computational Mathematics, Huayuan road 6, Beijing 100088, China
CAEP software Center for High Performance Numercial Simulation, Huayuan road 6, Beijing 100088, China
Dr X. Wang, Dr. P. Metz, Prof. K. Page
Department of Materials Science and Engineering, University of Tennessee, Knoxville, TN 37996, United States
Dr. C. A. Bridges
Chemical Sciences Division, Oak Ridge National Laboratory, Oak Ridge, Tennessee, 37831, United States

Keywords: *Ruddlesden-Popper, Local structure, interstitial oxygen, neutron total scattering, DFT, EXAFS*

The Ruddlesden-Popper (RP) layered-perovskite structure is of great interest due to its inherent tunability, and the emergence and growth of the compositionally complex oxide (CCO) concept endows the RP family with further possibilities. Here, a comprehensive assessment of thermodynamic stabilization, local order/disorder, and lattice distortion was performed in the first two reported examples of lanthanum-deficient $La_{n+1}B_nO_{3n+1}$ ($n = 1$, B = Mg, Co, Ni, Cu, Zn) obtained via various processing conditions. Chemical short-range order (CSRO) at the B-site and the controllable excess interstitial oxygen (δ) in RP-CCOs are uncovered by neutron pair distribution function (PDF) analysis. Reverse Monte Carlo (RMC) analysis of the data, Metropolis Monte Carlo simulations (MCS), and extended X-ray absorption fine structure (EXAFS) analysis implies a modest degree of magnetic element segregation on the local scale. Further, special quasirandom structure (SQS) models obtained by *ab initio* molecular dynamics simulations (AIMD) disagree with experimentally observed CSRO, but confirm Jahn-Teller distortion of CuO_6 octahedra. These findings highlight potential opportunities to control local order/disorder and excess interstitial oxygen in layered RP-CCOs, and demonstrate a high degree of freedom for tailoring application-specific properties. They also suggest a need for expansion of theoretical and data modeling approaches in order to meet the innate challenges of compositionally complex oxides and related high entropy phases.

1 Introduction

As an important class of layered perovskite oxides, the Ruddlesden-Popper (RP) $A_{n+1}B_nO_{3n+1}$ structure oxides have been considered for wide application in energy and electronic devices[1, 2, 3], such as solid oxide fuel cells (SOFC),[4] solar cells[5], electrocatalysis[6], and optoelectronics[7, 8]. The first and simplest structural archetype in the RP series, A_2BO_4 ($n = 1$ RP series), has recently attracted great interest owing to a diverse set of observed properties.[3] In general, the rare earth or alkaline earth metal elements occupy the A site (A = La, Pr, Nd, Sr, etc.), and the transition metal elements/divalent metal cations occupy

the B-site (B = Co, Ni, Fe, Cu, etc.).[9, 10] The A_2BO_4 compounds adopt two major phase forms: the T' (Nd_2CuO_4) phase with square-planar CuO_2 sheets and AO_8 cubes, and the T (K_2NiF_4) phase consisting of two-dimensional perovskite-like slabs interleaved with cations forming both BO_6 octahedra and AO_9 polyhedra.[11, 12] A number of recent studies have focused on doping strategies on the A-site or B-site in these layered perovskites for property enhancement.[3, 13, 4] Cation ordering in ABO_3 perovskites is known to bring interesting opportunities for tuning magnetic[14], electronic[15], and other properties, with B-site cations ordering more readily than A-site cations in general.[16, 17] The ionic radii, formal charge differences, and electrostatic forces among cations are the driving forces to ordering, while similar size, identical formal charge, and even increased configurational entropy from disordered cation arrangements may favor forming single phase solid solution structures.[18] Most studies in the literature have focused on cation ordering on the A-site in the RP A_2BO_4 phase[19, 20, 13, 4, 21], with comparatively few studies on the effects of B-site cation ordering.[19]

Among RP A_2BO_4 compounds, the La-based RP phase La_2BO_4 with different transition metals on the B-site has been most extensively studied and practically used. Previous studies from X-ray and neutron diffraction have shown that La_2BO_4 (B=Co, Ni, Cu) undergoes structural phase transitions from the high temperature T-tetragonal to low-temperature T-orthorhombic phase, and can feature excess interstitial oxygen (δ) (*ie.* $La_2NiO_{4+\delta}$).[22, 23, 24, 25, 26] The La_2CuO_4 compound has been found to involve a Jahn-Teller distortion with elongated CuO_6 octahedra and antiferromagnetic order.[27, 28, 29] La_2NiO_4 is antiferromagnetically ordered at room temperature, and oxygen-excess $La_2NiO_{4+\delta}$ phases show different symmetries depending on the synthesis conditions, the resulting oxygen stoichiometry, and the measurement temperature.[24, 30] La_2CoO_4 is also well documented to show antiferromagnetic long-range order at room temperature, and can easily be oxidized to $La_2CoO_{4+\delta}$ with δ values up to 0.25.[31, 32, 33, 34] The propensity for spontaneous oxidation at room temperature in the synthesis of $La_2CoO_{4+\delta}$ results in the typically undesired formation of Co^{3+}.[35, 36, 37] Substitution of Mg^{2+} or Zn^{2+} is known to induce simple magnetic dilution in the La_2BO_4 series.[38, 39] Some efforts have been made to synthesize La_2MgO_4 or La_2ZnO_4 compounds, but they are typically only found present as minor excess phases alongside more stable final products.[40, 41] More recently, Tidey et al. synthesized La_2MgO_4 through high pressure synthesis, resolving the origin of the well-known low-temperature orthorhombic (LTO) to low-temperature tetragonal (LTT) phase transition.[42]

High-entropy oxides (HEOs) have drawn much attention for their tunable functional properties and correspondingly remarkable potential in magnetic, catalytic and energy storage applications.[43, 44, 45, 46, 47, 48, 49, 50, 51, 52, 53, 54] HEOs are commonly defined as single phase oxides with a mixture of five or more cations in an equal or near-equal atomic ratio on a single crystallographic lattice site..[18] When the phase is stabilized by the resulting high configurational entropy the HEO is termed an entropy-stabilized oxide (ESO), as first observed via a reversible low temperature multiphase and high temperature single in rock salt oxide by Rost et al. in 2015.[55] There have been recent community efforts to clarify the definitions of low-, medium-, and high-entropy oxides;[56, 57] indeed, the RP phases in this work feature a maximum configurational entropy (S_{config}) of $0.69R$ (with R being the ideal gas constant). There is also growing recognition that many systems and variations will feature chemical short-range order, local atomic distortions, or other types of local atomic heterogeneity that lower or compete with S_{config} in the overall energy landscape of the materials classes. For these reasons, we refer to the RP phases herein as simply compositionally complex oxides (CCO) and affirm that variation in their local to long-range compositional complexity needs to be explored to fully understand them and how 'tunable' they may be. Some efforts have been made to explore configurational complexity on the A-site in RP A_2BO_4 phases and the influence of synthesis conditions, and no A-site ordering is observed through traditional X-ray crystallographic and electron microscopy techniques..[58, 13, 52] Recently, paracrystalline' B-site cation ordering was observed within $LaSr_3NiRuO_8$ planes below a correlation length scale of 6 Å by neutron total scattering. In addition, multipronged approaches including neutron total scattering, density functional theory (DFT)/*ab initio* molecular dynamics (AIMD) and Metropolis Monte Carlo simulations (MCS) were used to identify a strong local TiO_6 octahedral distortion and CSRO at the subnanometer length scale in $Nd_2M_2O_7$ pyrochlore HEO.[59]

Herein, we apply the high-entropy design principle to synthesize a new lanthanum-deficient Ruddlesden-Popper phase, $La_{2-x}(Mg_{0.2}Co_{0.2}Ni_{0.2}Cu_{0.2}Zn_{0.2})O_{4+\delta}$ (x= 0.1), which shows great potential for applications in energy conversion and electronic devices. We evaluate the ability to form a highly disordered mixture from thermodynamic phase stability calculations with different models for cation order in the RP-CCO phase. The local structure and formation of a single phase multicomponent compound are investigated using neutron diffraction, pair distribution function refinement with small-box and large-box methods, extended x-ray absorption fine structure (EXAFS) analysis, and Metropolis Monte Carlo simulations (MCS). DFT calculations were performed throughout this work in combination with thermodynamic analysis, special quasirandom structures (SQS) models, and MCS simulations. Finally, the cation order/disorder, excess interstitial oxygen (δ), lattice distortions, and magnetic properties in RP-CCOs are reported for the first time and in context of a slow cooling verses water quenching variation in sample preparation conditions.

2 Results and Discussion

2.1 Material synthesis

Two $La_{1.9}BO_{4+\delta}$ samples (where B is an equiatomic mixture of Mg, Co, Ni, Cu, and Zn) were synthesized by solid state reaction methods using distinct annealing protocols, as detailed in the Experimental Section. One sample was held at 1000 °C for 18 hours and then quenched into ice cold water (hereafter referred to RP-CCO, WQ). The second sample was held at 900 °C for 15 hours and slow cooled (5 °C/min) in the furnace (hereafter referred to RP-CCO, SC). Synthesis of the target RP phase without any impurity peaks was confirmed by powder diffraction and Rietveld refinement from neutron diffraction (Figure S1 and Figure 1a). Homogeneous distribution of the B-site cations at the micrometer length scale was confirmed be SEM-EDS (Figure 1b). High resolution STEM-EELS mapping was attempted for the samples (see WQ sample, Figure S2a). La, Co and Zn are readily observed, but the presence of lanthanum carbonates on the surfaces (for the Cu and Mg cases) and overlap with the La spectrum (for the Ni case) makes detection of the remaining atom types difficult. Preliminary analysis found that the magnitude of field cooling (FC) and magnetic field response measurements for WQ and SC samplesn are distinct, as shown in Figure 1c. However, fits to the Curie-Weiss law did not provide reasonable parameters, potentially caused by the presence of a weak impurity in the sample.

The RP-CCO phases at room temperature are indexed to the RT orthorhombic space group *Cmca* (No. 64); octahedral distortion prevented assignment in the HT tetragonal space group $I4/mmm$ (No. 139). This Space Group, is consistent with predictive metrics, as discussed in the following sections. Attempts were first made to complete Rietveld refinements with isotropic atomic displacement parameters (ADPs), producing large U_{iso} paramaters for the oxygen sites. Therefore, anisotopic ADPs were introduced for all the atoms, and lower goodness of fit values (R_w) were obtained. Inspection of Fourier difference nuclear density maps indicated evidence for an oxygen interstitial at (0.25, 0.25, 0.25) as O4 in both samples, as reported in $La_2CoO_{4+\delta}$ and $La_2Ni_{1-x}Cu_xO_{4+\delta}$ system [26, 60], and their inclusion improved R_w values for both samples (from 3.22% to 3.09% for WQ sample, and 3.77% to 3.60% for SC sample).

Final Rietveld refinement results using models with interstitial O4 oxygen resulted in high fit quality, and an overall stoichiometry of RP-CCO for the WQ sample and SC sample, as relayed in Figure 1b listed in Table S3. We noted that there is more oxygen at O4 for the SC sample than the WQ sample, suggesting that the slower cooling process enhances oxidation of the compounds. The oxygen interstitials and refined ADPs for the two samples are visualized in Figure S2b using 99% probability thermal ellipsoids. Of note, all U_{ij} components for O2 oxygen at 8f sites and the U_{22} component for O1 oxygen at the 8e sites result in large values, leading to 'rugby ball' shaped anisotropic displacement ellipsoids and implying significant local BO_6 octahedral distortions. These effects are more pronounced in the SC sample than in the WQ sample. Such features are of interest for their direct roles in influencing oxide-ion conductivity, catalytic ability, magnetic sublattice order, and other functional properties in RP phases.

2.2 Thermodynamic prediction and tolerance factor

There are two main criteria from the original Hume-Rothery solid-solution rules[61] that are often utilized to rationalize phase formation in studies of multi-component high-entropy alloys (HEAs).[62, 63, 64] The first criteria is the atomic size difference δ_{diff} defined as:

$$\delta_{diff}\% = 100\% \sqrt{\sum_{i=1}^{n} c_i \left(1 - \frac{r_i}{\sum_{i=1}^{n} c_i r_i}\right)^2} \quad (1)$$

Where c_i is the molar fraction and r_i is the atomic radius of the i-th element in the solid-solution or multi-component HEA. It is reasonable to assume the same formula may be extended to HEOs by replacing the individual atomic size differences with lattice constant (a, b and c) differences of the constituent single component metal oxides. In HEAs a reasonable value of δ_{diff} is found to be smaller than empirical criterion 6.6% [65], while the obtained values of δ_{diffa}, δ_{diffb} and δ_{diffc} for stoichiometric RP La_2BO_4 with B = Mg, Co, Ni, Cu and Zn (based on DFT relaxed cells) are a modest 1.0%, 1.8% and 1.7%, as seen in Table S1, respectively.

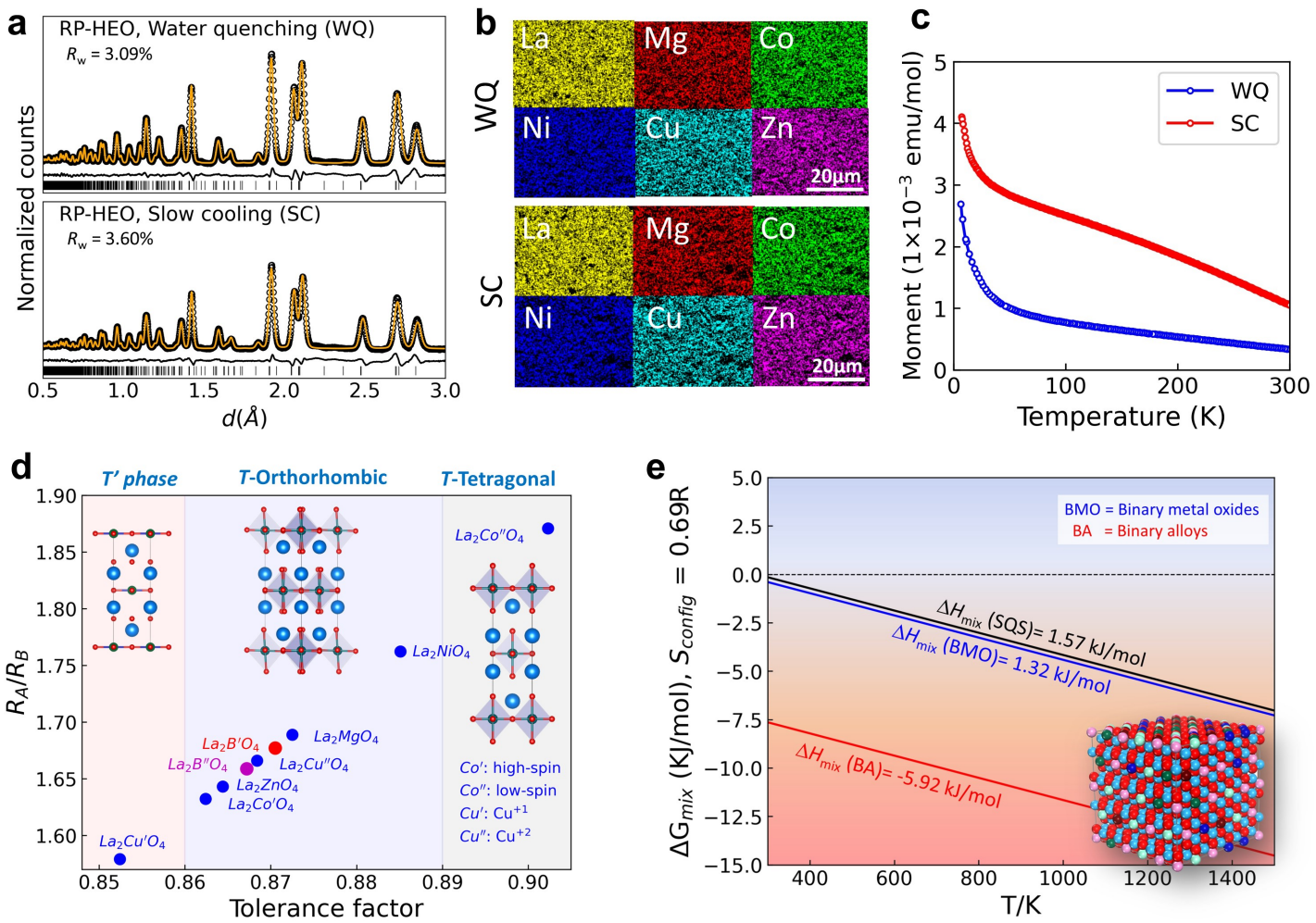

Figure 1: (**a**) Results of Rietveld analysis of neutron diffraction data with orthorhombic *Cmca* anisotropic atomic displacement model for RP-CCOs prepared via ice water quenching (WQ) and slow cooling (SC). (**b**) Energy dispersive X-ray spectroscopy (EDS) elemental mapping of La and B cations in RP-CCO samples. (**c**) Field cooling (FC) measurements with a magnetic field of 1000 Oe, and inverse magnetic susceptibility as a function of temperature for WQ and SC samples. (**d**) Tolerance factor versus the ionic radius ratio (R_A/R_B) of the A (La) and B cations of end member La_2BO_4 Ruddlesden-Popper phases (blue points), along with average values for the Cu^{2+} and Cu^{1+} (red and purple points, respectively). (**e**) Thermodynamic prediction of mixing Gibbs energy as a function of temperature for RP La_2BO_4 CCO from a regular solution model.

An alternative method to determine the stability of a single phase structure of an oxide is by developing

a tolerance factor 't'. The original Goldschmidt tolerance factor 't' developed to predict the stability of ABO_3 perovskite oxides based on the ionic radii of the A and B cations and oxygen remains in wide use.[66] This tolerance factor has additionally been used to rationalize the formation and crystal structure trends among mixed metal oxide RP phases, A_2BO_4, with success;[11] it is defined as follows:

$$t = \frac{r_A + r_B}{\sqrt{2}(r_B + r_O)} \tag{2}$$

Where r_A, r_B and r_O are the ionic radii of La^{3+} (1.16 Å) in 9-fold coordination, B cations (Mg^{2+} 0.72 Å, Co^{2+} high-spin 0.745 Å or Co^{2+} low-spin 0.65 Å, Ni^{2+} 0.69 Å, Cu^{1+} 0.77 Å or Cu^{2+} 0.73 Å, and Zn^{2+} 0.74 Å) in 6-fold coordination (note that Co^{2+} prefers a high-spin configuration in ground state La_2CoO_4[33], and Cu was designed to +1 in our samples), and oxygen (1.4 Å) in RP-CCO phase, respectively. The stability field for the T-orthorhombic and T-tegragonal phases is within the range $0.87 \leq t \leq 0.99$, and for the T' phase within the range $0.83 \leq t \leq 0.86$. The calculated tolerance factors for RP La_2BO_4 compounds with different B-site cation components is shown in Figure 1d, along with the predicted regions of stability for Nd_2CuO_4(T'), T-Orthorhombic, and T-Tetragonal phase regions. As can be seen, all individual B cation and average B cation in La_2MO_4 CCO tolerance factor values fall within the T-orthorhombic field, except for the high-spin configuration Co^{2+} end member, denoted as $La_2Co"O_4$, and end-members based on Ni^{2+} and low spin Co^{2+} cations. The above analysis of atomic lattice difference δ_{diff} values and RP phase tolerance factor 't' indicate that a stoichiometric RP La_2BO_4 (B= Mg^{2+}, Co^{2+}, Ni^{2+}, Cu^{2+}, Zn^{2+}) compound may readily form a single phase.

The second criteria commonly utilized to predict the formation of HEAs is the enthalpy of mixing ΔH_{mix}, which can be accessed from experimental studies or advanced thermodynamic calculations. Here, the enthalpy of mixing ΔH_{mix} of high entropy alloys is shown below:

$$\Delta H_{mix} = \sum_{i=1, i\neq j}^{n} \Omega_{ij} C_i C_j, \quad \Omega_{ij} = 4 \times \Delta H_{ij}^{mix} \tag{3}$$

Where ΔH_{ij}^{mix} denotes the mixing enthalpy of binary alloys of the i-th and j-th elements, and C_i and C_j denote the molar fraction of elements. The same formula can be extended to CCOs by replacing the pure metal element ΔH_{ij}^{mix}s with those of individual end member RP phases. We have calculated the ΔH_{BA}^{mix} from the binary alloys[67] as crude approximations, and compared the ΔH_{BO}^{mix} for the binary metal oxides from DFT calculations as shown in Figure S3 and Table S2. Furthermore, the ΔH_{SQS}^{mix} are calculated using different SQS configurations (Figure S4) to show a value as low as 1.57 kJ/mol. All the predicted mixing enthalpies are between -15 kJ/mol $< \Delta H_{mix} <$ 5 kJ/mol (empirical criterion to form stable high entropy solid solution),[61] which indicates a stable solid solution can be easily formed for compositionally complex La_2BO_4 RP oxides. Finally, we can calculate the mixing Gibbs free energy $\Delta G_{mix} = \Delta H_{mix} - T\Delta S_{mix}$, where ΔS_{mix} is the mixing entropy can be approximately equal to $\Delta S_{config} = 0.69R$ (R is the gas constant) as given for A_2BO_4.[68] The temperature dependent ΔG_{mix} obtained from different ΔH_{mix} are plotted in Figure 1e. Our preliminary thermodynamic analysis suggests that the stoichiometric RP-CCO is stable at RT, in agreement with our observation of single RP phases (albeit with processing dependent differences in overall oxygen stoichiometry). The extent to which the disparate processing conditions used in this work impact B cation charge, local CSRO, and other local lattice distortions is explored in the following sections.

2.3 Local structure analysis

Pair distribution function (PDF) methods from time-of-flight neutron total scattering data show a special ability to probe the local structure effectively. Figure 2a shows the neutron PDF patterns of both WQ and SC samples for RP-CCOs up to 50 Å. No significant differences in peak shapes and intensities were observed between WQ and SC samples. PDF refinements by small-box modeling using disordered unit-cell-based orthorhombic $Cmca$ models from Rietveld refinements (see Figure 2b for WQ sample) produces a fair fit with R_w of 0.084. A close inspection of the PDF fit reveals a small intensity mismatch near the first and

second B-O correlation length at low-r. On the basis of our previous experience with pyrochlore HEOs[59], this inconsistency may be derived from the disparate local environments of participating cations.

We have performed XPS analysis of the impact of sample processing conditions as shown in Figure S5. For both the WQ and SC samples, both the Mg 1s and Zn $2p_{3/2}$ show peaks that are assigned to Mg^{2+} and Zn^{2+}, respectively. The La 3d shows the typical main/satellite peak structure for the $3d_{5/2}$ and $3d_{3/2}$ when La is 3+ (as in La_2O_3). Weak peaks of Ni 3p were observed at near 68 eV, though due to the overlap of Ni 2p with the large La 3d core level spectra, the peaks were too weak to obtain a good measure of Ni content. Special attention was paid to collecting statistically significant data on the Cu and Co spectra, as it is expected that these are the most likely to show evidence of changes in oxidation state related to sample processing. The Co 2p are similar for both samples and are primarily due to Co^{2+}. However, the Cu $2p_{3/2}$ data show 2+ satellites between 942-947 eV, and a main peak at $\sim$ 933 eV indicating Cu 1+, suggesting a mixture of Cu^{2+} and Cu^{1+}. The ratio of Cu 2+ satellites to the Cu $2p_{3/2}$ peaks is 0.21 for WQ and 0.29 for SC, and after Ar-ion etching, the ratios are 0.21 and 0.28 for WQ and SC, respectively. The XPS data indicate that the La/Mg/Co/Ni/Zn spectra appear unaffected by sample processing, while the Cu 2+ spectra are affected: slow cooling appears to result in a more oxidized sample, with a higher concentration of Cu^{2+}, than is observed in the quenched sample. This result is consistent with the findings from the Rietveld refinement analysis above. Furthermore, prior work on La_2CuO_4[69] has shown that synthesis in air results in a slightly reduced phase of $La_2CuO_{3.85}$, which can be converted to stoichiometric La_2CuO_4 at 500 °C under 600 psi of O_2. For these high entropy samples, the presence of Cu^{1+} shows that it is energetically favorable for the sample to remain somewhat reduced at high temperature, and that slow-cooling in air is not sufficient to fully oxidize the Cu to 2+.

Disordered unit-cell-based models cannot distinguish individual B atom pair-pair correlations resulting from a refinement, while the DFT optimized SQS model can provide details of local cation environments for a given simulated random configuration[70, 59]. The DFT relaxed SQS model has been used successfully to model pyrochlore HEOs in our previous work, which decomposed the partial neutron PDFs from individual B-O pair-pair correlations successfully.[59] Five optimal SQSs (on the basis of a totally random configuration) were used here to fit the PDF data of the WQ sample as shown in Figure S6. The fits using the SQS models do not reproduce the experimental PDF data perfectly; they provide worse agreement to data than the *Cmca* model with average B site occupancies. The fitting results of one SQS configuration, with corresponding partial PDFs are shown in Figure 2c and 2f. We note that the intensity mismatch from the B-O correlation remains and the first La-O pair-pair correlation displays a strongly non-Gaussian distribution, indicating that the oxygen displacements from the average structure positions vary according to the specific B-site cation involved in the SQS model. This result may indicate that the real RP-CCO compounds feature less cation-specific local distortion than predicted by SQS or that the small SQS model used here is not perfectly disordered (it is not large enough to be representative of the real system). Alternatively (or in addition), it is plausible the model is a poor representation because the real RP-CCO compounds are nonstoichiometric with lanthanum-deficiency and feature oxygen vacancies and interstitials. Computational demands of DFT when using large supercells limits further studies using SQS models with these features.

Large-box reverse Monte Carlo (RMC) simulations using RMCProfile[71] software are carried out to analyze the statistical distribution of specific atoms in multicomponent systems[72, 73, 74, 59]. As shown in Figure 2d and 2g for the WQ sample, the RMC approach provides a high quality fit to experimental neutron PDF data over the whole PDF fitting range, and simultaneously fits the associated normalized structure factor data, F(Q), and Bragg data (see more details in Figure S7 and S8 for RMC refinements with and without B site cation atom-swapping for both WQ and SC samples). Calculated partial PDFs from the RMC model are shown in Figure S9. Similar quality fits were obtained for both WQ and SC samples. Note that the low-r fits are significantly improved as compared with disordered *Cmca* and SQS model results. Unlike the DFT-relaxed SQS models confined to a small number of atoms, the RMC models with tens of thousands of atoms can produce all possible local atomic environments consistent with fitting various data types simultaneously and adhering to imposed constraints. Although there is a modest driving force for cation disorder associated with maximizing configurational entropy and forming a single

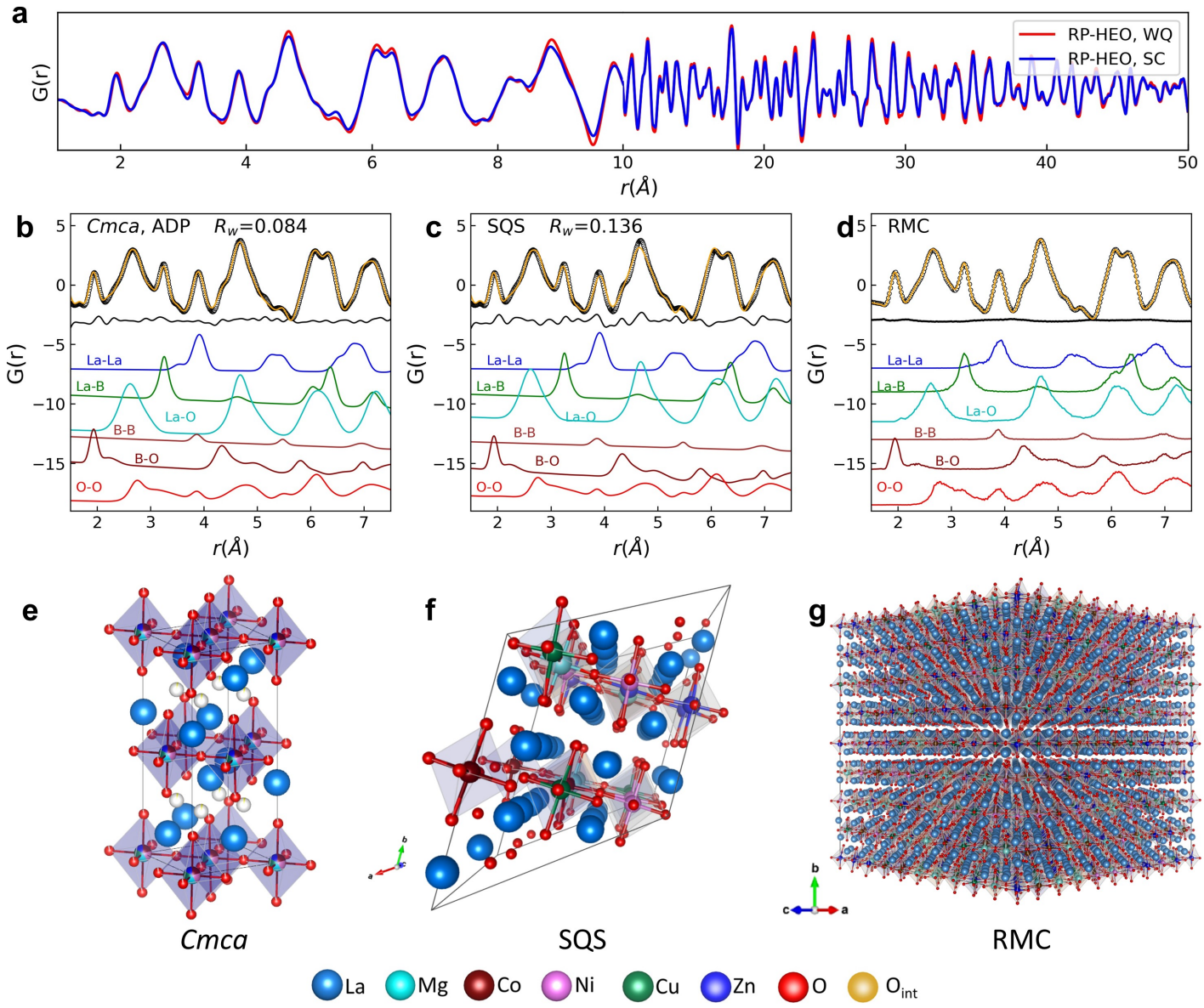

Figure 2: (**a**) Comparison of PDFs, G(r), for RP-CCOs prepared via ice water quenching (WQ) and slow cooling (SC). Note the G(r) is shown with an expanded r-axis below 10/,Åto highlight subtle intensity differences. Experimental G(r) (black circles), model fits (orange circles) and simulated partial PDFs (colored lines) for WQ sample computed from (**b**) a small-box model using the B-site mixed disordered orthorhombic *Cmca* structure shown in (**e**), (**c**) a SQS model after full DFT relaxation corresponding to the structure shown in (**f**), and (**d**) a 10×4×10 supercell RMC model of orthorhombic *Cmca* containing 11200 atoms shown in (**g**).

solid solution phase in CCOs, there is a possibility of existence of local cation ordering due to crystal chemical factors such as cation size and charge difference, local bond valence, magnetic ordering, tolerance factor[17], and diffusion limits of specific synthesis/processing conditions. The built-in atom-swapping algorithm[75] in RMCProfile was performed to search for evidence of local CSRO in the RP-CCO samples. It should be noted that the fitting for G(r) data are moderately improved by including the atom-swapping, which indicates some extent of cation ordering across the B sites.

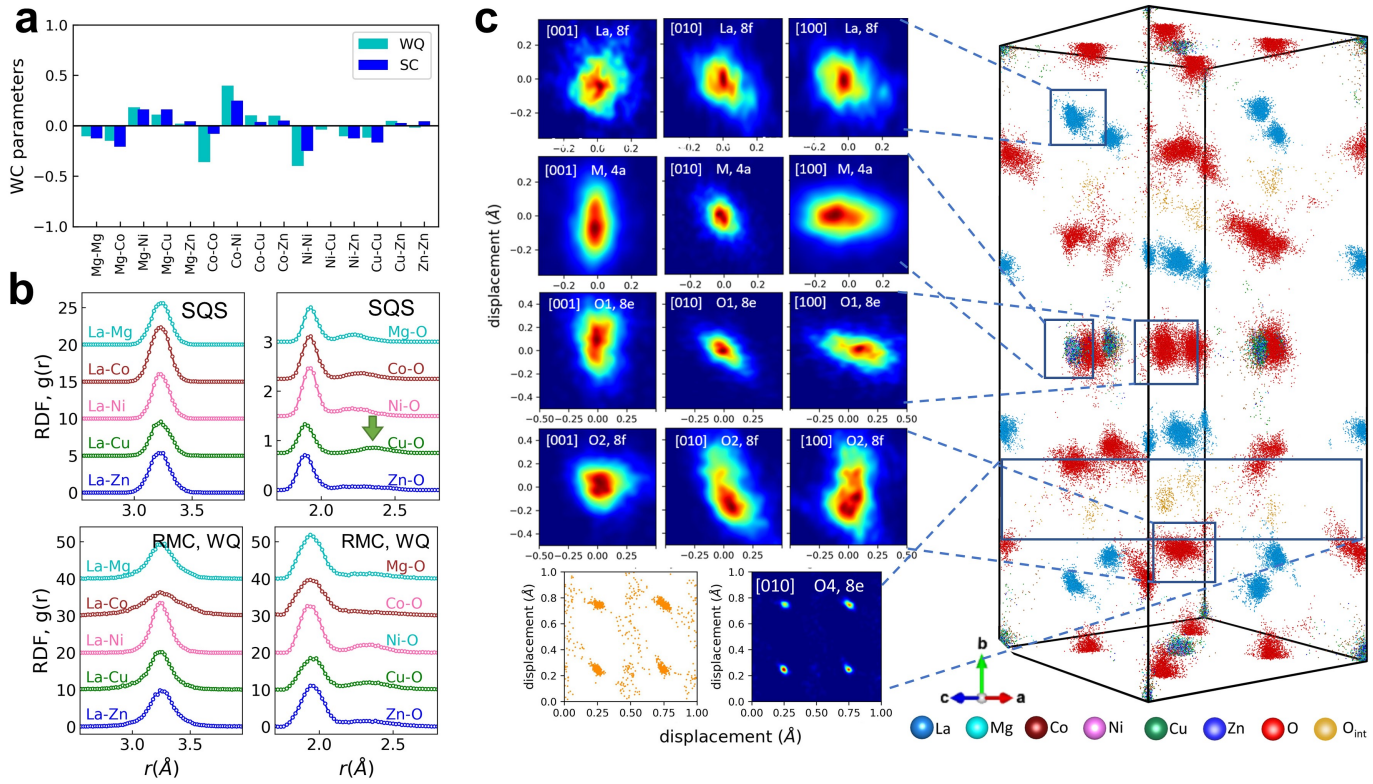

Figure 3: (**a**) The Warren-Cowley (WC) parameters of second shell correlations for WQ and SC samples from the RMC fits. (**b**) The first La-B and B-O pair-pair correlation peaks from the model of AIMD-SQS and RMC simulations for the WQ sample. (**c**) Folded point clouds from 10 independent RMC models and corresponding select density plots (left) of La (8f), B cations (4a), oxygen (8e and 8f) and interstitial $O_{4,int}$(8e) displayed along different directions for the WQ sample.

The B-site cation ordering after RMC refinement can be quantified by nearest neighbor function $n_{ij}(r)$ [76, 75] and Warren-Cowley (WC)[77, 78] parameters, as shown in Figure S10, S11 and Figure 3a. This analysis reveals important variation in WQ and SC samples. In the SC sample there is less variation among the $n_{ij}(r)$ and WC values of B-site cation pairs for first- and second-neighbor correlations, indicating a trend towards a *more* random distribution with the slow cooling treatment. This suggests that configurational entropy does not play a dominant role in determining B-site cation order in the samples/conditions studied here. Note that the RMC atom-swapping introduces some modest cation-cation pair segregation or clustering for pairs such as Co-Co, Ni-Ni and Co-Ni pairs (indicated with higher/lower $n_{ij}(r)$ and WC parameters) . It is noted these are magnetically active cations, expected to display weak antiferromagnetic interactions in their diluted state within the La_2BO_4 lattice.[33] It is possible that antiferromagnetic coupling interactions have provided a driving force for modest cation segregation.

This uncovered local CSRO in RP-CCOs is consistent with the B-O correlation length intensity mismatch in the disordered *Cmca* and DFT relaxed SQS fits. Further study on the comparison of La-B and B-O pairs between the AIMD-SQS and RMC simulations for the WQ sample are shown in Figure 3b, revealing that the final model outcomes were greatly affected by the modeling strategies and included data types. We can see that the partial radial distribution functions (RDFs) from AIMD-SQS simulation for all B-O pairs are found to be similar, apart from a first bond length difference. Note that the second

Cu-O bond length peak shows a deviation from other B-O (green arrow in Figure 3b), which suggests Jahn-Teller (JT) distortion as seen in rocksalt ESO[79]. However, this JT distortion feature might not be obvious from RMC modeling, which has limited chemical resolution due to the high number of elements in RP-CCOs, as discussed in our previous paper[59]. Moreover, a broad distribution of La-Co and Co-O pairs are observed from RMC modeling which may be partly explained by the lower value for the neutron scattering length of Co (2.49 fm) or the interstitial oxygen located on tetragonal lattice sites around Co^{3+}. Close inspection of folded RMC point clouds of individual cation and oxygen distributions at different sites in Figure 3d (more details in Figure S12-S14) reveals similar results to the ADP distribution from Rietveld refinements in Figure S2b. Note that La cation clouds show more spheroidal distributions than B site cations. The enlarged distribution of equatorial O1 and apical O2 positions indicates that the large distortion in local BO_6 octahedral eenvironments is due to mixing multiple cations, while interstitial O4 oxygen diffuses in layered RP phase. However, no significant shape differences in point cloud distributions are observed among these five B-site cations (Mg, Co, Ni, Cu, Zn) for both WQ and SC samples (Figure S13 and S14) with neutron total scattering models.

2.4 EXAFS analysis and Metropolis Monte Carlo Simulations.

To verify the detected local cation ordering, the EXAFS spectra were collected for Co, Ni, Cu and Zn at K-edges for the WQ sample at beamline 10-BM-B at APS as shown in Figure 4a (Note that the Mg K-edge is not accessible at 10-BM-B), the raw data are given in Supplementary Figure S15. Samples were measured in fluorescence mode with 10 scans averaged to improve the signal-to-noise ratio. The similarity between k-space spectra (Figure 4a) demonstrate the similar local environments of each cation in the RP-CCOs. R-space spectra are provided in Figure 4b and show peaks for the local B-O environment and the first several B-B pair correlations. Note that the pair distance denoted is not readily interpretable as a distance in EXAFS, as the peak position is modified by a backscattering phase-shift. The similar positions and shapes of first and second main peaks for all cations indicates similar local bonding environments in the solid solution. However, there is a slight shift to the right of the first peak for the Zn atom which could indicate a distinct local bonding environment (note there are no reports of pure Zn RP phases). In addition, there are some subtle differences between spectra that may suggest some degree of difference in the local oxygen and B-B environments for each cation. This is most strongly seen in the intensity of the B-O peak and the separation between the B-O and B-B peaks, which is indicative of differences in the local oxygen environments and B-O coordination number. The B-O peak for Co is particularly high in intensity, which is suggestive of a higher B-O coordination number due to interstitial oxygen (consistent with previously reported results for $La_2CoO_{4+\delta}$)[31, 32, 33, 34]. However, highly parameterized modeling of the EXAFS is precluded by the relatively short k-range of the data collected. The k-range is fundamentally limited by the energy difference between the absorption edges of the elements present in the RP-CCOs.

In our recent works we utilized Metropolis Monte Carlo simulations (MCS) to predict the phase stability and cation disorder of high entropy oxides in the rock salt[80] and pyrochlore[59] structures. In this work, we utilize a similar methodology to predict the local $B-$site disorder in stoichiometric compositionally complex RP La_2BO_4 (see MCS supercell in Figure 4c and related analysis details in Figure S16 and S17). Figure 4d and 4e compare the $n_{B-B}(r)$ value for the first nearest neighbors of Co related pairs from RMC modelling, and the right panel shows corresponding MCS simulation results of Co related $n_{B-B}(r)$ as a function of r and T (shown in Figure 4f and 4g, see all values for first, second and third nearest neighbors in Figure S18, respectively). Each $B-$site is surrounded by 4 $B^{'}-$sites for the first and second nearest B neighbors, and 8 $B^{'}-$sites for the third nearest B neighbors. Since each $B-$site can be occupied by one of five cations, at ideal disorder, $n^{NN1}_{B-B'} = n^{NN2}_{B-B'} = \frac{4}{5} = 0.8$ and $n^{NN3}_{B-B'} = \frac{8}{5} = 1.6$. The ideal disorder value is represented in each panel by a black dashed line. We find that, as the temperature increases, all CSRO parameters tend towards ideal disorder. Owing to the low formation enthalpy of La_2CoO_4, we find that Co is prone to strongly segregate at lower temperatures compared to other cations. At $T > 800$ K, Co mixes with other cations and forms a disordered RP structure. All other cations, Cu, Mg, Ni and Zn tend to mix with each other relatively easily even at lower temperatures $T > 600$ K. This result is partly consistent with the modest Co-related CSRO uncovered via RMC simulations. Nonetheless, it is noted

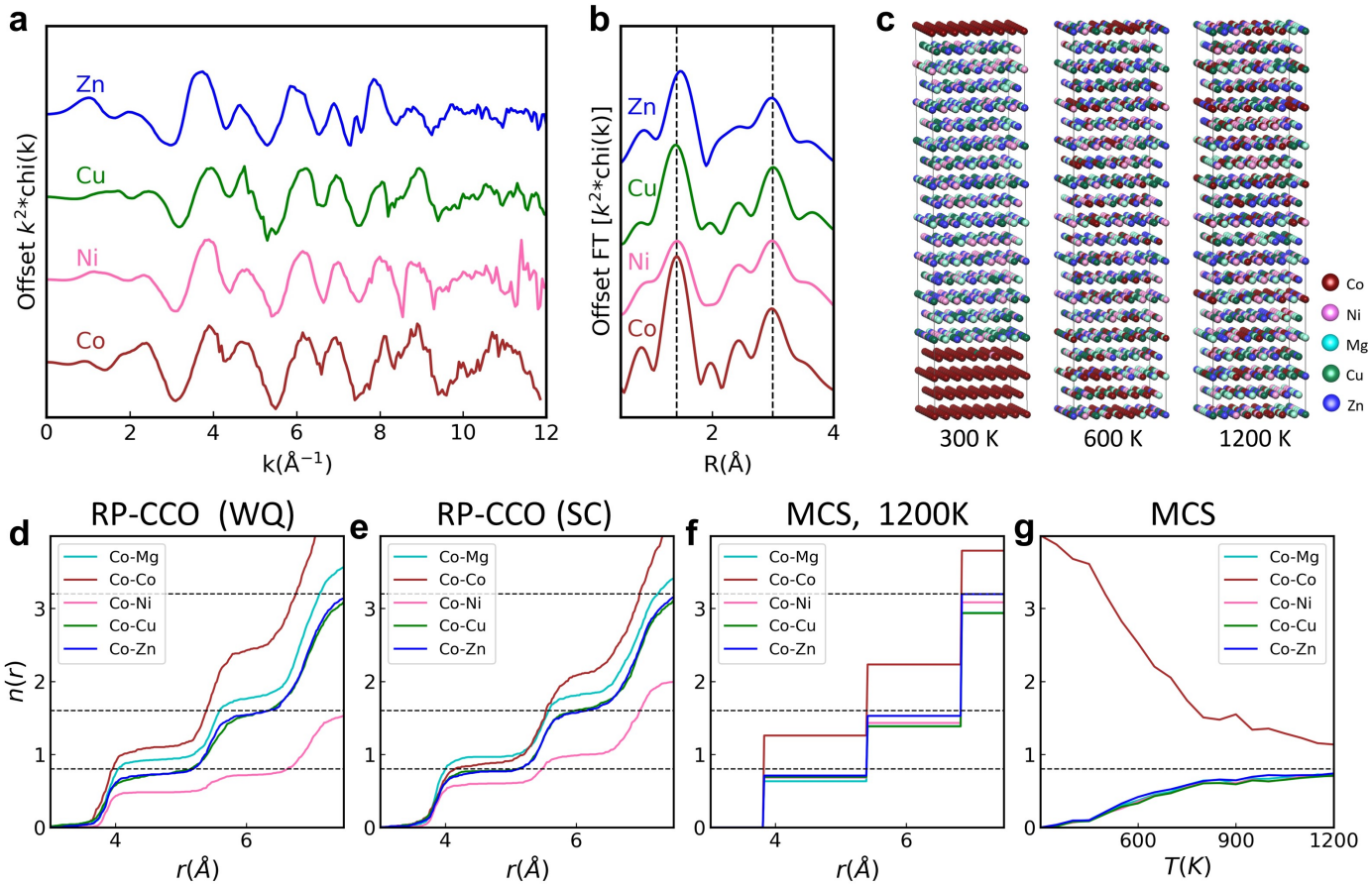

Figure 4: (**a**) metal K-edge EXAFS measured at Advanced Photo Source beamline 10-BM-B in fluorescence mode for WQ sample. (**b**) R-space EXAFS Fourier-transform magnitude plots for each element. (**c**) MCS simulation supercell. (**d, e**) Nearest-neighbor functions $n_{B-B}(r)$ of Co-B displaying the local cation ordering of B-site cation of RMC modeling in RP-CCOs of WQ and SC samples. The dashed lines show the theoretical $n_{A-A}(r)$ values for a statistically disordered distribution. MCS simulation shows (**f**) Nearest-neighbor functions $n_{B-B}(r)$ of Co-B at 1200 K and (**g**) the variation of first nearest-neighbor with respect to temperature.

that the MCS modeling predicts a greater propensity for mixing (disorder) on RP cation lattice sites at high temperatures, yet the work herein indicates that the SC sample results in a more disordered cation configuration than the WQ sample annealed at higher temperature and for longer annealing time. The simplicity of the fixed lattice cluster expansion energy model in MCS simulations cannot be ignored in regards to this complex RP-CCO phase. The effects of multiple Cu charge states, La and O vacancies, and oxygen interstitials, for example, are not considered. It is likely that multiple such factors combine to drive the particular CSRO behavior observed experimentally in RP-CCOs. Further studies will be needed to explore the system and understand its complex crystal chemistry and tunability.

3 Conclusion

In summary, we report an experimental and theoretical investigation of a new family of compositionally complex RP $La_{1.9}BO_{4+\delta}$ (B = Mg, Co, Ni, Cu and Zn) oxides obtained via quenching from high temperature and slow cooling. The thermodynamic phase stability, and the experimentally determined local and average structures, excess interstitial oxygen (δ) levels, and local lattice distortions have been studied in detail. The thermodynamic criteria and tolerance factor confirm that there is a tendency to have a disordered solid solution RP-CCO with homogeneous B-site cation distribution, which is consistent with the single phase x-ray and neutron diffraction analysis. However, a large positional disorder of oxygen, BO_6

octahedral distortion, and local CSRO are identified by PDF analyses using small-box PDFgui and large-box RMC modelling, departing from DFT/AIMD simulations using relaxed SQS. EXAFS quantitative analysis reveals similar local chemical environments for B-site cations, with a higher oxygen coordination environment detected for Co atoms. Further MCS simulations reveal that cobalt has a higher preference towards phase segregation at lower temperatures than other cations, consistent with the segregation or clustering for magnetic cations. Finally, diffraction and XPS analysis demonstrate that slow cooling results in a significant increase in disorder and oxidization in these RP-CCOs. Finding less cation segregation suggests that configurational disorder (the thermodynamic benefit of which will be decreased at lower synthesis temperatures and through slow cooling) does not play a dominant structure-directing role in the formation of the specific RP-CCOs here. On the other hand, the observation of a single phase structure that flexibly accommodates multiple valence states (like in the copper-based RP end-member phases) as well as significant interstitial oxygen content (like in the Co-based RP end-member phases) is a demonstration of the 'cocktail' effect intrinsic to the high entropy materials construct. Overall, these comprehensive results are valuable as an indicator that new compositionally complex RP perovskites and related phases may be designed with targeted properties through variation in synthesis and processing conditions, for example, towards new optoelectronic or ferroelectric materials. Finally, we note that despite all the methods we have used to characterize and analyze this compositionally complex material, there remain unresolved characterization and design challenges that highlight a need for new developments in model techniques and model parameters that can distinguish the structural traits intrinsic to high entropy oxides and the larger compositionally complex oxide family.

4 Experimental Section

Sample synthesis: Starting materials of La_2O_3, CoO, MgO, Cu_2O, NiO and ZnO were weighed in stoichiometric amounts. Due to the presence of La_2O_3 in reaction products with stoichiometric amounts of lanthanum precursor, we used a 5 % deficiency, which was sufficient to produce a pure compound according to laboratory X-ray diffraction data. Reagents were ground together in a mortar and pestle, and then milled together to produce a homogeneous mixture in a plastic vial with YSZ balls using a SPEX 8000 mill. The resulting powder was pressed into pellets, loaded into alumina crucibles, and heated to 850 °C at 5 °C/minute in air. The pellets were held at 850 °C for 3 hours, and then heated at 5 °C/minute to different final temperatures. One sample was held at 1000 °C for 18 hours and then quenched into ice cold water (hereafter referred to RP-CCO, WQ). The second sample was held at 900 °C for 15 hours and slow cooled (5 °C/min) in the furnace (hereafter referred to RP-CCO, SC).

Lab X-ray Powder Diffraction, scanning and transmission electron microscopy: X-ray diffraction data were collected on powder samples on zero background holders using a Panalytical Empyrian diffractometer with Cu Ka radiation (Figure S1). The surface structure of the synthesized RP-CCO was analyzed using a scanning electron microscope (Zeiss Auriga crossbeam FIB/SEM). The elemental distribution of the samples was determined by using energy-dispersive X-ray spectroscopy (EDS) in conjunction with a scanning electron microscope (ZEISS EVO SEM). High resolution STEM coupled with EELS was used to examine the morphology and elemental concentration of the samples. EELS spectra were analyzed using the Gatan software suite with corrections for multiple scattering and peak overlap.

Magnetometry measurements: Magnetic susceptibility measurements were performed using an MPMS SQUID magnetometer, using powders contained within gel caps. Zero-field cooling (ZFC) and field cooling (FC) data were collected in the temperature range of 2 to 300 K for the SC sample, while ZFC data were collected for the WQ sample down to 6K. In both cases, data were collected in a field of 1000 Oe.

X-ray photoelectron spectroscopy(XPS): XPS data were collected using a Thermo Scientific (Waltham, MA, USA) Model K-Alpha XPS instrument, using monochromated, micro-focused, Al Kα X-rays (1486.6 eV) with a variable spot size (i.e., 30-400 µm). Analyses of the sample was performed with the 400 µm X-ray spot size for maximum signal and to obtain an average surface composition over the largest possible area. Due to significant sample charging, several sample mounting approaches were attempted, with the

optimum data being collected by pressing the powder into a stand-alone pellet that was attached to the XPS holder with carbon tape. Survey spectra (pass energy = 200 eV) were acquired for qualitative and quantitative analysis and high-resolution core level spectra (pass energy = 50 eV) were acquired for detailed chemical state analysis. All spectra were acquired with the charge neutralization flood gun turned on to maintain a stable analysis condition. Data from Ar-ion etched surfaces (30 seconds etching) were collected for comparison. In some cases slight peak shifts and distortions are observed due to charging, though multiple data sets were collected in order to better determine the intrinsic spectra. Data were collected and processed using the Thermo Scientific Avantage XPS software package (v.5.96). Peak fitting was performed using mixed Gaussian/Lorentzian peak shapes and a Shirley/Smart type background.

Neutron total scattering: PDF G(r) were collected on the NOMAD instrument,[81] at the Spallation Neutron Source (SNS) at Oak Ridge National Laboratory. Neutron total scattering data from four banks were reduced within the ADDIE software[82]. The initial average structures were obtained from Rietveld refinement using TOPAS v6 software [83] with the orthorhombic *Cmca* structure for RP-CCOs. The following parameters were refined in the Rietveld analysis: scale factor, profile parameters, unit cell parameters, background parameters, atomic positions, isotropic/anisotropic atomic displacements, and site occupancies (occ) for interstitial oxygen. The experimental PDF data were subsequently analyzed by least-squares 'small-box' modeling using PDFgui [84]. 'Large-box' Reverse Monte Carlo (RMC) simulations of PDFs were performed with the RMCprofile software[71] using a $10\times4\times10$ supercell of orthorhombic *Cmca* structure. Finally, the RMC model was obtained by fitting PDF G(r), scattering function F(Q), and the neutron diffraction patterns simultaneously. In all RMC simulations, bond valence sum (BVS) restrictions were applied to avoid unphysical bond lengths. The B cations were allowed to swap places within the lattice. Each simulation ran for more than 2000 minutes on one 3.2GHz core CPU, generating about 2.0×10^7 moves. A total of 10 final RMC configurations were produced for each sample and the results were combined for further analysis.

EXAFS measurements and analysis: The complex local structure of compositionally complex oxides makes unique structural determination by total scattering a difficult problem. The element specific local structure given by EXAFS is a powerful tool in understanding CSRO in complex oxides.[55, 79] XAS spectra of the WQ RP-CCO sample was measured at the MRCAT bending magnet line (10-BM-B) of the Advanced Photon Source (APS) at Argonne National Laboratory.[85] Measurements were performed in fluorescence mode using a vortex 4 element solid state detector. Powder samples were pressed into a self-supporting pellet angled 45 degrees relative to the x-ray beam, with the fluorescence detector positioned 90 degrees relative to the incident beam. Spectra were collected at the K edges of Co, Zn, Ni and Cu (the Mg K edge is not accessible at 10-BM-B). Each edge was scanned 10 times and averaged to improve signal to noise ratio. No systematic changes were observed between averaged scans. Data reduction and analysis was performed using the Demeter software suite[86].

DFT-SQS Calculations: Density functional theory (DFT) calculations were carried out using the plane-wave-based Vienna Ab initio Simulation Package VASP[87, 88], within the generalized gradient approximation (GGA) using the Perdew-Burke-Ernzerhof for solids (PBEsol) exchange-correlation functional.[89]. The standard PBE PAW potentials La($5s^25p^65d^16s^2$), Co($3d^74s^2$), Ni($3p^63d^94s^1$), Mg($2p^63s^2$), Cu($3p^63d^{10}4s^1$), Zn($3d^{10}4s^2$) and O($1s^22p^4$) were used here. The plane waves were expanded up to a cutoff energy of 560 eV and specifically selected Hubbard U values of 10, 5.0, 5.1, 4.5, and 7.5 were applied to La, Co, Ni, Cu, and Zn, as reported in [90]. Brillouin zone integration was done on a $8\times4\times8$ k-point mesh grid for the single orthorhombic *Cmca* La_2BO_4 phase with 28 atoms. Full geometry optimizations were performed until the Hellman-Feynman forces on the atoms were relaxed below 10^{-2} eV/Å[91]. The magnetic ground state for magnetic cations (Co, Ni and Cu) were initialized with antiferromagnetic (AFM) ordering in concordance with the magnetic ordering of bulk $La_2CoO_{4+\delta}$.

The special quasirandom structures (SQS)[92] of RP La_2MO_4 were prepared by the 'mcsqs' utility (Monte Carlo generator of SQS) in the Alloy Theoretic Automated Toolkit (ATAT) [93, 94]. The SQS

method was used here to generate a random distribution of M-site disorder in periodic supercells. A Metropolis Monte Carlo algorithm was applied to randomly exchange the atomic positions of M-site atoms[94]. Multiple supercells were examined and the the optimal SQS was selected as the one with the minimum deviation from the completely random pairwise and triplet correlations to first, second, and third nearest neighbors (NN) distance. The models selected are plotted in Figure S4.

Brillouin zone integrations were completed with a density of at least 20 k-points $Å^{-1}$ for DFT calculations of SQS supercells in this work. *Ab initio* molecular dynamics (AIMD) simulations using the NVT ensemble [95] were carried out via the algorithm of Nosé [96] to control the temperature oscillations during the DFT calculations. Brillouin zone integration was completed on a single gamma-centered k-point and the cut off energy was reduced to 450 eV for all AIMD calculations. Each AIMD simulation was run for 5000 steps at 300 K with a time-step of 2 fs. The last 3000 steps were used to generate the time averaged structure at each temperature.

MCS simulation details: Metropolis Monte Carlo simulations (MCS) have been used in this paper in combination with DFT calculations. DFT calculations were carried out in order to estimate mixing enthalpies using VASP as described above. The energy cutoff for the plane-wave basis set was 800 eV, employing projected augmented wave potentials.[97, 88] A $4\times4\times4$ $k-$point mesh was utilized for sampling the Brillouin zone for a $2 \times 2 \times 1$ supercell containing 8 $B-$sites in the La_2BO_4 unit cell and scaled linearly with the number of atoms present in the unit cell. The bulk geometry was optimized with a force convergence criterion of 2 meV/Å, and the individual components of the stress tensor were converged to $\leq$ 0.1 kB. Magnetism of Co, Ni, and Cu containing structures was treated with the PBEsol collinear spin density approximation in the GGA with an onsite Hubbard U (GGA+U) scheme.[98] An on-site Coulomb parameter $U = 6$ eV was applied for these cations to account for the increased Coulomb repulsion between the semi-filled $3d$ states. In our previous computational investigation of (CoCuMgNiZn)O, we used the same values of U and exchange correlation functional to model the high entropy oxide in the rock salt structure.[80] An in-plane checkered antiferromagnetic ordering is initiated for the magnetic cations.

The pairwise mixing enthalpies $\Delta H_{\text{mix}}[La_2(BB')O_4]$ in generic two component perovskite structure, $La_2(BB')O_4$ is given by:

$$\begin{aligned}\Delta H_{\text{mix}}[La_2(BB')O_4] = E_{\text{DFT}}[La_2(BB')O_4] - E_{\text{DFT}}[La_2O_3, \text{G}] \\ - \frac{1}{x}E_{\text{DFT}}[BO, \text{G}] - \frac{1}{1-x}E_{\text{DFT}}[B'O, \text{G}]\end{aligned} \tag{4}$$

where $E_{\text{DFT}}[La_2(BB')O_4]$, $E_{\text{DFT}}[La_2O_3, \text{G}]$, $E_{\text{DFT}}[BO, \text{G}]$, $E_{\text{DFT}}[B'O, \text{G}]$, are the total energies of two component perovskite, La_2O_3, BO, and $B'O$ oxides in their ground state phase structures. x and $1 - x$ are the atomic fractions of B and B' cations respectively.

In this work we have considered a $2\times2\times1$ supercell (containing 8 $B-$sites), which allows us to estimate the mixing enthalpies for $x = \{0, \frac{1}{8}, \frac{1}{4}, \frac{1}{2}, \frac{3}{4}, \frac{7}{8}, 1\}$, where $x = 0$ or $x = 1$ represent pure RP structures. In the case of $x = \{\frac{1}{8}, \frac{7}{8}\}$ the cations can be ordered in only one way, whereas for $x = \{\frac{1}{4}, \frac{3}{4}\}$, and $x = \{\frac{1}{2}\}$, we have considered two and three cation ordered configurations, respectively. For example, in the case of $x = \frac{1}{2}$, there are 4 cations each of B and B', which can be arranged with (i) checkered order within (001) planes, (ii) layered ordering — B and B' cations occupying adjacent (001) planes, and (iii) striped order — stripes of B and B' cations within the (001) planes. The cation orderings discussed above are presented in the Supporting Information. For each two-component combination we generate 9 different atomic configurations of varying degree of atomic fractions and cation ordering. Since there are 10 different two component combinations, we generate 90 atomic configurations of two component and 5 end member (one component) RP structures. Figure S16 plots the values of the mixing enthalpies for all two component compositions. The left most and right most columns represent the mixing enthalpies of pure RP-structures with $B-$sites mentioned adjacent to their columns.

We employed Metropolis Monte Carlo simulations to study the mixing behavior between different chemical species within the five component RP structure, at relevant temperatures ranging from $T = 300$ to 1200 K with a temperature step of $\Delta T = 50$ K. Atomic configurations — generated through randomly

swapping unlike atoms between different lattice sites in a $8 \times 8 \times 10$ periodic supercell (containing 1280 $B-$sites) — are sampled according to the Metropolis criterion. The simulation is started from a random atomic configuration. A trial configuration is accepted according to the Boltzmann probability, p_B

$$p_B = \text{Minimum}\left\{\exp\left(\frac{-\Delta H}{k_B T}\right), 1\right\} \tag{5}$$

where, $\Delta H = \Delta H_n^{\text{total}} - \Delta H_{n-1}^{\text{total}}$ is the change in total mixing enthalpy between n and $n-1$ steps, caused by swapping unlike chemical species, k_B is the Boltzmann constant and T is the absolute temperature. The trial configuration is always accepted if $\Delta H \leq 0$. However, if $\Delta H > 0$ the trail configuration is accepted by chance according to the Boltzmann probability, p_B. The RP-structure is highly anisotropic due to the presence of ABO_3 perovskite layers, separated by the AO rock salt layer along the $\langle 0, 0, 1\rangle$ direction. Hence in order to capture the anisotropic $B - B^{'}$ interactions, we have utilized a cluster expansion (CE) energy model as implemented in Alloy Theoretic Automated Toolkit (ATAT) open source software.[93, 99]

The total energy, H^{total}, of a microstate is obtained from the CE model. $B - B^{'}$ interactions up to the third nearest neighbors — the first, second nearest neighbors are in-plane interactions and the third nearest neighbor is the out-of-plane interaction — are considered in the CE model. The CE model was trained using the cationic configurations featuring 90 two-component and 5 pure RP structures. Figure S17 plots the values of CE vs DFT mixing enthalpies for all 95 configurations. We find good correlation between DFT and CE mixing enthalpies. The value of the short-range order parameters $\text{n}_{B-B'}^{NNi}$ for the first ($NN1$), second ($NN2$) and third ($NN3$) nearest neighbors of a microstate is estimated by averaging the number of atoms of species $B^{'}$ surrounding all atoms of species B. By the commutative relation, $\text{n}_{B-B'}^{NNi} = \eta_{B'-B}^{NNi}$ there are 15 unique short-range order parameters each for $NN1$, $NN2$ and $NN3$ in the five-component high-entropy RP-structure.

Nearest neighbor function $n_{ij}(r)$ and Warren-Cowley parameters: The B-site cation ordering from simulations or refinement models can be expressed in terms of the nearest neighbor function $n_{ij}(r)$ [76, 75]. The $n_{ij}(r)$ is defined as the mean number of atoms i surrounding a central atom j; $n_{ij}(r) = \int_{r2}^{r1} 4\pi r^2 2 c_j \rho_0 g_{ij}(r)\, dr$, where c_j is the proportion of atom j in the compound, ρ_0 is the average number density of the compound, and g_{ij} is the partial pair distribution function for atoms i and j. The Warren-Cowley (WC) parameters[77, 78] were applied to describe CSRO in this RP-CCO system, more details can be found in the supporting information in our recent paper https://doi.org/10.1021/jacs.0c10739.

Acknowledgements

Material compositions evaluation, synthesis and initial theory work were supported by the Laboratory Directed Research and Development (LDRD) Program of Oak Ridge National Laboratory, managed by UT-Battelle, LLC, for the U.S. DOE. Work by V.R.C. and C.A.B. after 2020 was funded by the U.S. Department of Energy, Office of Science, Basic Energy Sciences, Materials Sciences and Engineering Division. Work by K.P. after 2021 was funded by a National Science Foundation CAREER Award, Division of Materials Research, Solid State Chemistry Program. This research used the NOMAD beamline at the Spallation Neutron Source, a DOE Office of Science User Facility operated by the Oak Ridge National Laboratory. MRCAT operations are supported by the Department of Energy and the MRCAT member institutions. This research used resources of the Advanced Photon Source, a U.S. Department of Energy (DOE) Office of Science User Facility operated for the DOE Office of Science by Argonne National Laboratory under Contract No. DE-AC02-06CH11357. The computing resources were made available through the VirtuES project as well as the Compute and Data Environment for Science (CADES) at Oak Ridge National Laboratory, which is supported by the Office of Science of the U.S. Department of Energy under Contract No. DE-AC05-00OR22725. We thank Charl J. Jafta for his valuable contributions to discussions.

References

[1] S. Ruddlesden, P. Popper, Acta Crystallographica **1958**, 11, 1 54.

[2] I. B. Sharma, D. Singh, Bulletin of Materials Science **1998**, 21, 5 363.

[3] G. Nirala, D. Yadav, S. Upadhyay, Journal of Advanced Ceramics **2020**, 9, 2 129.

[4] P. Ding, W. Li, H. Zhao, C. Wu, L. Zhao, B. Dong, S. Wang, Journal of Physics: Materials **2021**, 4, 2 022002.

[5] C. Liang, D. Zhao, Y. Li, X. Li, S. Peng, G. Shao, G. Xing, Energy & Environmental Materials **2018**, 1, 4 221.

[6] X. Xu, Y. Pan, Y. Zhong, R. Ran, Z. Shao, Materials Horizons **2020**, 7, 10 2519.

[7] Y. Chen, Y. Sun, J. Peng, J. Tang, K. Zheng, Z. Liang, Advanced Materials **2018**, 30, 2 1703487.

[8] X. Gao, X. Zhang, W. Yin, H. Wang, Y. Hu, Q. Zhang, Z. Shi, V. L. Colvin, W. W. Yu, Y. Zhang, Advanced Science **2019**, 6, 22 1900941.

[9] J. Song, D. Ning, B. Boukamp, J.-M. Bassat, H. J. Bouwmeester, Journal of Materials Chemistry A **2020**, 8, 42 22206.

[10] H. Zhao, Q. Li, L. Sun, Science China Chemistry **2011**, 54, 6 898.

[11] J. F. Bringley, S. S. Trail, B. A. Scott, Journal of Solid State Chemistry **1990**, 86, 2 310.

[12] B.-H. Chen, Journal of Solid State Chemistry **1996**, 125, 1 63.

[13] B. L. Musicó, Q. Wright, C. Delzer, T. Z. Ward, C. J. Rawn, D. G. Mandrus, V. Keppens, Journal of the American Ceramic Society **2021**, 104, 7 3750.

[14] R. Rawl, M. Lee, E. S. Choi, G. Li, K.-W. Chen, R. Baumbach, C. Dela Cruz, J. Ma, H. Zhou, Physical Review B **2017**, 95, 17 174438.

[15] Y. Bu, O. Gwon, G. Nam, H. Jang, S. Kim, Q. Zhong, J. Cho, G. Kim, Acs Nano **2017**, 11, 11 11594.

[16] G. King, P. M. Woodward, Journal of Materials Chemistry **2010**, 20, 28 5785.

[17] P. Davies, H. Wu, A. Borisevich, I. Molodetsky, L. Farber, Annu. Rev. Mater. Res. **2008**, 38 369.

[18] J.-W. Yeh, S.-K. Chen, S.-J. Lin, J.-Y. Gan, T.-S. Chin, T.-T. Shun, C.-H. Tsau, S.-Y. Chang, Advanced Engineering Materials **2004**, 6, 5 299.

[19] J. A. Rodgers, P. D. Battle, N. Dupré, C. P. Grey, J. Sloan, Chemistry of materials **2004**, 16, 22 4257.

[20] P. Battle, M. Green, N. S. Laskey, J. Millburn, L. Murphy, M. Rosseinsky, S. Sullivan, J. Vente, Chemistry of materials **1997**, 9, 2 552.

[21] M. Garali, M. Kahlaoui, B. Mohammed, A. Mater, C. ben Azouz, C. Chefi, International Journal of Hydrogen Energy **2019**, 44, 21 11020.

[22] J. Longo, P. Raccah, Journal of Solid State Chemistry **1973**, 6, 4 526.

[23] T. Kajitani, S. Hosoya, K. Hiraga, T. Fukuda, Journal of the Physical Society of Japan **1990**, 59, 2 562.

[24] J. Rodriguez-Carvajal, M. T. Fernandez-Diaz, J. L. Martinez, Journal of Physics: Condensed Matter **1991**, 3, 19 3215.

[25] L. Minervini, R. W. Grimes, J. A. Kilner, K. E. Sickafus, Journal of Materials Chemistry **2000**, 10, 10 2349.

[26] A. Aguadero, J. A. Alonso, L. Daza, Zeitschrift für Naturforschung B **2008**, 63, 6 615.

[27] Y. Yamaguchi, H. Yamauchi, M. Ohashi, H. Yamamoto, N. Shimoda, M. Kikuchi, Y. Syono, Japanese journal of applied physics **1987**, 26, 4A L447.

[28] S. Cheong, J. Thompson, Z. Fisk, Physica C: Superconductivity **1989**, 158, 1-2 109.

[29] C. Lane, J. W. Furness, I. G. Buda, Y. Zhang, R. S. Markiewicz, B. Barbiellini, J. Sun, A. Bansil, Physical Review B **2018**, 98, 12 125140.

[30] H. Tamura, A. Hayashi, Y. Ueda, Physica C: Superconductivity **1993**, 216, 1-2 83.

[31] J. T. Lewandowski, R. A. Beyerlein, J. M. Longo, R. A. McCAULEY, Journal of the American Ceramic Society **1986**, 69, 9 699.

[32] R. M. Ram, P. Ganguly, C. Rao, J. Honig, Materials research bulletin **1988**, 23, 4 501.

[33] K. Yamada, M. Matsuda, Y. Endoh, B. Keimer, R. Birgeneau, S. Onodera, J. Mizusaki, T. Matsuura, G. Shirane, Physical Review B **1989**, 39, 4 2336.

[34] A. Demourgues, F. Weill, B. Darriet, A. Wattiaux, J. Grenier, P. Gravereau, M. Pouchard, Journal of Solid State Chemistry **1993**, 106, 2 330.

[35] R. Le Toquin, W. Paulus, A. Cousson, G. Dhalenne, A. Revcolevschi, Physica B: Condensed Matter **2004**, 350, 1-3 E269.

[36] L. Le Dreau, C. Prestipino, O. Hernandez, J. Schefer, G. Vaughan, S. Paofai, J. M. Perez-Mato, S. Hosoya, W. Paulus, Inorganic chemistry **2012**, 51, 18 9789.

[37] Ş. Ortatatlı, J. Ternieden, C. Weidenthaler, European Journal of Inorganic Chemistry **2018**, 2018, 48 5238.

[38] A. Chakraborty, A. J. Epstein, M. Jarrell, E. McCarron, Physical Review B **1989**, 40, 7 5296.

[39] S. Cheong, A. Cooper, L. Rupp Jr, B. Batlogg, J. Thompson, Z. Fisk, Physical Review B **1991**, 44, 17 9739.

[40] U. Kameswari, C. Swamy, Journal of materials science letters **1985**, 4, 12 1515.

[41] D. Reinen, J. Wegwerth, Physica C: Superconductivity **1991**, 183, 4-6 261.

[42] J. P. Tidey, C. Keegan, N. C. Bristowe, A. A. Mostofi, Z.-M. Hong, B.-H. Chen, Y.-C. Chuang, W.-T. Chen, M. S. Senn, arXiv preprint arXiv:2111.11888 **2021**.

[43] C. Oses, C. Toher, S. Curtarolo, Nature Reviews Materials **2020**, 5, 4 295.

[44] B. L. Musicó, D. Gilbert, T. Z. Ward, K. Page, E. George, J. Yan, D. Mandrus, V. Keppens, APL Materials **2020**, 8, 4 040912.

[45] Y. Ma, Y. Ma, Q. Wang, S. Schweidler, M. Botros, T. Fu, H. Hahn, T. Brezesinski, B. Breitung, Energy & Environmental Science **2021**, 14, 5 2883.

[46] A. Sarkar, L. Velasco, D. Wang, Q. Wang, G. Talasila, L. de Biasi, C. Kübel, T. Brezesinski, S. S. Bhattacharya, H. Hahn, et al., Nature communications **2018**, 9, 1 1.

[47] A. Sarkar, Q. Wang, A. Schiele, M. R. Chellali, S. S. Bhattacharya, D. Wang, T. Brezesinski, H. Hahn, L. Velasco, B. Breitung, Advanced Materials **2019**, 31, 26 1806236.

[48] R.-Z. Zhang, M. J. Reece, Journal of Materials Chemistry A **2019**, 7, 39 22148.

[49] Y. Sun, S. Dai, Science Advances **2021**, 7, 20 eabg1600.

[50] H. Xiang, Y. Xing, F.-z. Dai, H. Wang, L. Su, L. Miao, G. Zhang, Y. Wang, X. Qi, L. Yao, et al., Journal of Advanced Ceramics **2021**, 10, 3 385.

[51] A. Sarkar, R. Kruk, H. Hahn, Dalton Transactions **2021**, 50, 6 1973.

[52] A. R. Mazza, E. Skoropata, Y. Sharma, J. Lapano, T. W. Heitmann, B. L. Musico, V. Keppens, Z. Gai, J. W. Freeland, T. R. Charlton, et al., Advanced Science **2022**, 2200391.

[53] P. R. Jothi, W. Liyanage, B. Jiang, S. Paladugu, D. Olds, D. A. Gilbert, K. Page, Small **2022**, 18, 5 2101323.

[54] X. Wang, B. L. Musicó, C. Kons, P. C. Metz, V. Keppens, D. A. Gilbert, Y. Zhang, K. Page, APL Materials **2022**, 10, 12 121102.

[55] C. M. Rost, E. Sachet, T. Borman, A. Moballegh, E. C. Dickey, D. Hou, J. L. Jones, S. Curtarolo, J.-P. Maria, Nature communications **2015**, 6, 1 1.

[56] S. J. McCormack, A. Navrotsky, Acta Materialia **2021**, 202 1.

[57] M. Brahlek, M. Gazda, V. Keppens, A. R. Mazza, S. J. McCormack, A. Mielewczyk-Gryń, B. Musico, K. Page, C. M. Rost, S. B. Sinnott, et al., APL Materials **2022**, 10, 11 110902.

[58] W. Zhang, A. R. Mazza, E. Skoropata, D. Mukherjee, B. Musico, J. Zhang, V. M. Keppens, L. Zhang, K. Kisslinger, E. Stavitski, et al., ACS nano **2020**, 14, 10 13030.

[59] B. Jiang, C. A. Bridges, R. R. Unocic, K. C. Pitike, V. R. Cooper, Y. Zhang, D.-Y. Lin, K. Page, J. Am. Chem. Soc. **2021**, 143, 11 4193.

[60] A. Aguadero, J. Alonso, M. Escudero, L. Daza, Solid State Ionics **2008**, 179, 11-12 393.

[61] Y. Zhang, T. T. Zuo, Z. Tang, M. C. Gao, K. A. Dahmen, P. K. Liaw, Z. P. Lu, Progress in Materials Science **2014**, 61 1.

[62] Y. Ye, Q. Wang, J. Lu, C. Liu, Y. Yang, Materials Today **2016**, 19, 6 349.

[63] Y. Zhang, Y. J. Zhou, J. P. Lin, G. L. Chen, P. K. Liaw, Advanced Engineering Materials **2008**, 10, 6 534.

[64] F. Tian, L. K. Varga, N. Chen, J. Shen, L. Vitos, Intermetallics **2015**, 58 1.

[65] X. Yang, Y. Zhang, Materials Chemistry and Physics **2012**, 132, 2-3 233.

[66] V. Goldschmidt, S. N. Videnskaps-Akad, I. Oslo, Mat. Nat. Kl **1926**, 8.

[67] A. Dębski, R. Dębski, W. Gąsior, Archives of Metallurgy and Materials **2014**, 59.

[68] O. F. Dippo, K. S. Vecchio, Scripta Materialia **2021**, 201 113974.

[69] D. Johnston, J. Stokes, D. Goshorn, J. Lewandowski, Physical Review B **1987**, 36, 7 4007.

[70] B. K. Voas, T.-M. Usher, X. Liu, S. Li, J. L. Jones, X. Tan, V. R. Cooper, S. P. Beckman, Physical Review B **2014**, 90, 2 024105.

[71] M. G. Tucker, D. A. Keen, M. T. Dove, A. L. Goodwin, Q. Hui, Journal of Physics: Condensed Matter **2007**, 19, 33 335218.

[72] L. Owen, H. Playford, H. Stone, M. Tucker, Acta Materialia **2016**, 115 155.

[73] L. Owen, E. Pickering, H. Playford, H. Stone, M. Tucker, N. Jones, Acta Materialia **2017**, 122 11.

[74] S. Y. Chong, R. J. Szczecinski, C. A. Bridges, M. G. Tucker, J. B. Claridge, M. J. Rosseinsky, Journal of the American Chemical Society **2012**, 134, 13 5836.

[75] Q. Hui, M. T. Dove, M. G. Tucker, S. A. Redfern, D. A. Keen, Journal of Physics: Condensed Matter **2007**, 19, 33 335214.

[76] D. A. Keen, Journal of Applied Crystallography **2001**, 34, 2 172.

[77] J. Cowley, Physical Review **1950**, 77, 5 669.

[78] J. Cowley, Physical Review **1965**, 138, 5A A1384.

[79] C. M. Rost, Z. Rak, D. W. Brenner, J.-P. Maria, Journal of the American Ceramic Society **2017**, 100, 6 2732.

[80] K. C. Pitike, K. C. Santosh, M. Eisenbach, C. A. Bridges, V. R. Cooper, Chem. Mater. **2020**, 32, 17 7507.

[81] J. Neuefeind, M. Feygenson, J. Carruth, R. Hoffmann, K. K. Chipley, Nuclear Instruments and Methods in Physics Research Section B: Beam Interactions with Materials and Atoms **2012**, 287 68.

[82] M. McDonnell, D. Olds, K. Page, J. Neufeind, M. Tucker, J. Bilheux, W. Zhou, P. Peterson, Acta Crystallogr., Sect. A: Found. Adv **2017**, 73 a377.

[83] A. A. Coelho, Journal of Applied Crystallography **2018**, 51, 1 210.

[84] C. Farrow, P. Juhas, J. Liu, D. Bryndin, E. Božin, J. Bloch, T. Proffen, S. Billinge, Journal of Physics: Condensed Matter **2007**, 19, 33 335219.

[85] A. Kropf, J. Katsoudas, S. Chattopadhyay, T. Shibata, E. Lang, V. Zyryanov, B. Ravel, K. McIvor, K. Kemner, K. Scheckel, et al., In AIP Conference Proceedings, volume 1234. American Institute of Physics, **2010** 299–302.

[86] B. Ravel, M. Newville, Journal of synchrotron radiation **2005**, 12, 4 537.

[87] G. Kresse, J. Furthmüller, Physical review B **1996**, 54, 16 11169.

[88] G. Kresse, D. Joubert, Physical review b **1999**, 59, 3 1758.

[89] J. P. Perdew, A. Ruzsinszky, G. I. Csonka, O. A. Vydrov, G. E. Scuseria, L. A. Constantin, X. Zhou, K. Burke, Physical review letters **2008**, 100, 13 136406.

[90] Z. Rak, C. Rost, M. Lim, P. Sarker, C. Toher, S. Curtarolo, J.-P. Maria, D. Brenner, Journal of Applied Physics **2016**, 120, 9 095105.

[91] H. Mao, Y. Wei, H. Gui, X. Li, Z. Zhao, W. Xie, Journal of Applied Physics **2014**, 115, 21 213910.

[92] A. Zunger, S.-H. Wei, L. Ferreira, J. E. Bernard, Physical Review Letters **1990**, 65, 3 353.

[93] A. Van De Walle, Calphad **2009**, 33, 2 266.

[94] A. Van de Walle, P. Tiwary, M. De Jong, D. Olmsted, M. Asta, A. Dick, D. Shin, Y. Wang, L.-Q. Chen, Z.-K. Liu, Calphad **2013**, 42 13.

[95] R. Windiks, B. Delley, The Journal of chemical physics **2003**, 119, 5 2481.

[96] S. Nosé, The Journal of chemical physics **1984**, 81, 1 511.

[97] P. E. Blöchl, Physical review B **1994**, 50, 24 17953.

[98] S. L. Dudarev, G. A. Botton, S. Y. Savrasov, C. J. Humphreys, A. P. Sutton, Phys. Rev. B **1998**, 57 1505.

[99] A. van de Walle, G. Ceder, J. Phase Equilib. **2002**, 23, 4 348.